



# Magnetolectric Effect in Hydrogen Harvesting: Magnetic Field as a Trigger of Catalytic Reactions

## Journal Article

### Author(s):

Kim, Donghoon; [Efe, Ipek](#) ; Torlakcik, Harun; Terzopoulou, Anastasia; Veciana, Andrea; Siringil, Erdem; Mushtaq, Fajer; Franco, Carlos; von Arx, Denis; Sevim, Semih; Puigmarti-Luis, Josep; [Nelson, Bradley](#) ; Spaldin, Nicola A.; Gattinoni, Chiara; Chen, Xiang-Zhong; Pané, Salvador

### Publication date:

2022-05-12

### Permanent link:

<https://doi.org/10.3929/ethz-b-000543228>

### Rights / license:

[Creative Commons Attribution-NonCommercial 4.0 International](#)

### Originally published in:

Advanced Materials 34(19), <https://doi.org/10.1002/adma.202110612>

### Funding acknowledgement:

771565C - Highly Integrated Nanoscale Robots for Targeted Delivery to the Central Nervous System (EC)

764977 - Advanced integrative solutions to Corrosion problems beyond micro-scale: towards long-term durability of miniaturized Biomedical, Electronic and Energy systems (EC)

190451 - 3D Magnetic Nanoparticle Assemblies for Tumor-Targeted Nanomedicine: a Microrobotic Approach (SNF)

810451 - Hidden, entangled and resonating orders/HERO (EC)

# Magnetoelectric Effect in Hydrogen Harvesting: Magnetic Field as a Trigger of Catalytic Reactions

Donghoon Kim, Ipek Efe, Harun Torlakcik, Anastasia Terzopoulou, Andrea Veciana, Erdem Siringil, Fajer Mushtaq, Carlos Franco, Denis von Arx, Semih Sevim, Josep Puigmartí-Luis, Bradley Nelson, Nicola A. Spaldin, Chiara Gattinoni,\* Xiang-Zhong Chen,\* and Salvador Pané\*

Magnetic fields have been regarded as an additional stimulus for electro- and photocatalytic reactions, but not as a direct trigger for catalytic processes. Multiferroic/magnetoelectric materials, whose electrical polarization and surface charges can be magnetically altered, are especially suitable for triggering and control of catalytic reactions solely with magnetic fields. Here, it is demonstrated that magnetic fields can be employed as an independent input energy source for hydrogen harvesting by means of the magnetoelectric effect. Composite multiferroic  $\text{CoFe}_2\text{O}_4\text{-BiFeO}_3$  core-shell nanoparticles act as catalysts for the hydrogen evolution reaction (HER), which is triggered when an alternating magnetic field is applied to an aqueous dispersion of the magnetoelectric nanocatalysts. Based on density functional calculations, it is proposed that the hydrogen evolution is driven by changes in the ferroelectric polarization direction of  $\text{BiFeO}_3$  caused by the magnetoelectric coupling. It is believed that the findings will open new avenues toward magnetically induced renewable energy harvesting.

electrocatalytic processes.<sup>[3–5]</sup> For example, magnetic fields can be used to engineer the spin polarization of magnetic catalysts so that the catalysts and chemical adsorbents have coherent spin states, improving electron transfer efficiency between catalysts and chemical adsorbents. This results in faster kinetics and significantly increased catalytic activities in the hydrogen evolution reaction (HER)<sup>[6–8]</sup> and the oxygen evolution reaction (OER).<sup>[9,10]</sup> However, whether a magnetic field can be employed as the sole trigger of hydrogen energy harvesting is still unanswered despite of the advantages of deep penetration depth, low noise and damage, and flexibility in control parameters (i.e., magnitude and frequency) that magnetic fields offer.

Multiferroic and magnetoelectric nanocomposites provide opportunities for exploiting magnetic fields as a direct

trigger for hydrogen production.<sup>[11–14]</sup> While magnetic fields can influence the motion of electrons in magnetic materials, they cannot generate internal electric fields nor charges that are necessary for catalytic reactions. In contrast, magnetoelectric coupling occurs in multiferroic magnetoelectric composite materials when a magnetic field is applied. In typical strain-mediated magnetoelectric composites, the magnetic component responds to magnetic fields and transfers the magnetostrictive

## 1. Introduction

Magnetic fields have been extensively investigated as catalytic reaction boosters to enhance photocatalytic and electrocatalytic performances for clean energy production.<sup>[1,2]</sup> Adding magnetic components to current catalysts allows magnetic fields to play a significant role in carrier and mass transportation in catalytic systems and can enhance the efficiency of photo- and


D. Kim, H. Torlakcik, A. Terzopoulou, A. Veciana, E. Siringil, F. Mushtaq, C. Franco, D. Arx, S. Sevim, B. Nelson, X.-Z. Chen, S. Pané  
Multi-Scale Robotics Lab  
Institute of Robotics and Intelligence Systems  
ETH Zürich  
Tannenstrasse 3, Zürich CH-8092, Switzerland  
E-mail: chen@mavt.ethz.ch; vidalp@ethz.ch

I. Efe, N. A. Spaldin, C. Gattinoni  
Materials Theory  
Department of Materials  
ETH Zürich  
Wolfgang-Pauli-Strasse 27, Zürich 8093, Switzerland  
E-mail: gattinoc@lsbu.ac.uk

J. Puigmartí-Luis  
Departament de Ciència dels Materials i Química Física  
Institut de Química Teòrica i Computacional  
University of Barcelona (UB)  
Barcelona 08028, Spain

J. Puigmartí-Luis  
Institució Catalana de Recerca i Estudis Avançats (ICREA)  
Pg. Lluís Companys 23  
Barcelona 08010, Spain

C. Gattinoni  
Department of Chemical and Energy Engineering  
London South Bank University  
103 Borough Rd, London SE1 0AA, UK

 The ORCID identification number(s) for the author(s) of this article can be found under <https://doi.org/10.1002/adma.202110612>.

© 2022 The Authors. Advanced Materials published by Wiley-VCH GmbH. This is an open access article under the terms of the Creative Commons Attribution-NonCommercial License, which permits use, distribution and reproduction in any medium, provided the original work is properly cited and is not used for commercial purposes.

DOI: 10.1002/adma.202110612

strain to the ferroelectric/piezoelectric component by interfacial interaction.<sup>[15,16]</sup> The resulting change in electric polarization generates surface charges, which can ultimately induce catalytic reactions if the magnetoelectric material is interfaced with an electrolyte. In this report, we demonstrate magnetically induced HER using multiferroic core-shell nanoparticles for the first time. Hydrogen evolution was observed on applying alternating magnetic fields to magnetoelectric nanoparticles dispersed in aqueous solutions. Our first-principles density functional calculations suggest that magnetic field induced changes in the direction of the ferroelectric polarization cause the generation of charge carriers at the surface, which in turn promotes the catalytic reactions.

## 2. Results and Discussion

Magnetoelectric  $\text{CoFe}_2\text{O}_4\text{-BiFeO}_3$  (CFO-BFO) core-shell nanoparticles have been employed as a heterogeneous magnetoelectric-HER catalyst. CFO was chosen for the magnetostrictive core because it is known to have a very high magnetostriction coefficient (max. 600 ppm).<sup>[17,18]</sup> CFO core particles were synthesized using co-precipitation and hydrothermal methods and coated with a BFO shell using a sol-gel method. The crystalline structure of the as-synthesized CFO-BFO core-shell nanoparticles was analyzed with X-ray diffraction (Figure 1a). The Rietveld refinement confirms the presence of crystalline CFO and BFO, having cubic Fd-3m and hexagonal R3c space groups, respectively, without any secondary phase (the optimized parameters and the reliability parameters of the Rietveld refinement are provided in Table S1, Supporting Information). The high-angle annular dark-field scanning transmission electron microscopy (HAADF-STEM) and corresponding energy-dispersive X-ray spectroscopy (EDX) mappings clearly confirm the core-shell nature of the nanoparticles with a CFO core, containing Co, Fe, and O, and a BFO shell with Bi, Fe, and O elements (Figure 1b–g). The estimated core size and the shell

thickness of the synthesized CFO-BFO core-shell nanoparticles are  $35 \pm 8$  and  $4 \pm 1.5$  nm, respectively. As-synthesized CFO-BFO nanoparticles possess good piezoelectric and magnetoelectric properties, which are confirmed by the piezoresonance force microscopy (PFM) (Figure 2). A representative atomic force microscopy (AFM) topography, PFM amplitude, and phase images are provided in Figure S1, Supporting Information. The clear phase contrast in Figure S1, Supporting Information, indicates different polarization directions existing in the core-shell nanoparticles. Under the application of 50 mT DC in-plane magnetic field, local piezoelectric hysteresis loops showed noticeable magnetoelectric coupling in CFO-BFO nanoparticles, as evidenced by the large shifts of positive and negative coercive voltages from 2.61 to 1.51 V and from  $-3.88$  to  $-3.04$  V, respectively. In addition, the piezoelectric response also increased under the magnetic field (Figure 2). We propose the quantity  $\alpha_E = \Delta E / \Delta H$  as a measure of the magnetoelectric coupling in the nanoparticles, where  $\Delta H$  is the increment of the external magnetic field and  $\Delta E$  is the increment of the induced electric field, as previously reported.<sup>[19]</sup> In this case, 50 mT (500 Oe) of external magnetic field induced an electric field of  $(1.10 \text{ V} - 0.84 \text{ V}) / 2 / 8 \text{ nm} = 16.25 \text{ MV m}^{-1}$ . Therefore, the calculated magnetoelectric coefficient of the CFO-BFO core-shell nanoparticle is  $\alpha_E = 32.5 \times 10^4 \text{ mV cm}^{-1} \text{ Oe}^{-1}$ , which is comparable to previously reported values.<sup>[13]</sup>

Magnetically driven HER via the core-shell nanoparticles was then measured using an online gas chromatography (GC) setup under 22.3 mT, 1.19 kHz AC magnetic field (details of the measurement setup can be found in Figures S2 and S3, Supporting Information). When the particles were dispersed in deionized (DI) water (10 mg/10 mL),  $4.01 \mu\text{mol g}^{-1}$  of hydrogen was produced after 6 h (Figure 3a). To reveal the field-dependent performance, experiments were conducted for 8 h in total and the magnetic field was turned off for 2 h during which no hydrogen evolution was observed. In addition, we tested control samples under the same magnetic field (deionized (DI) water, CFO nanoparticles + DI water, CFO nanoparticles + DI

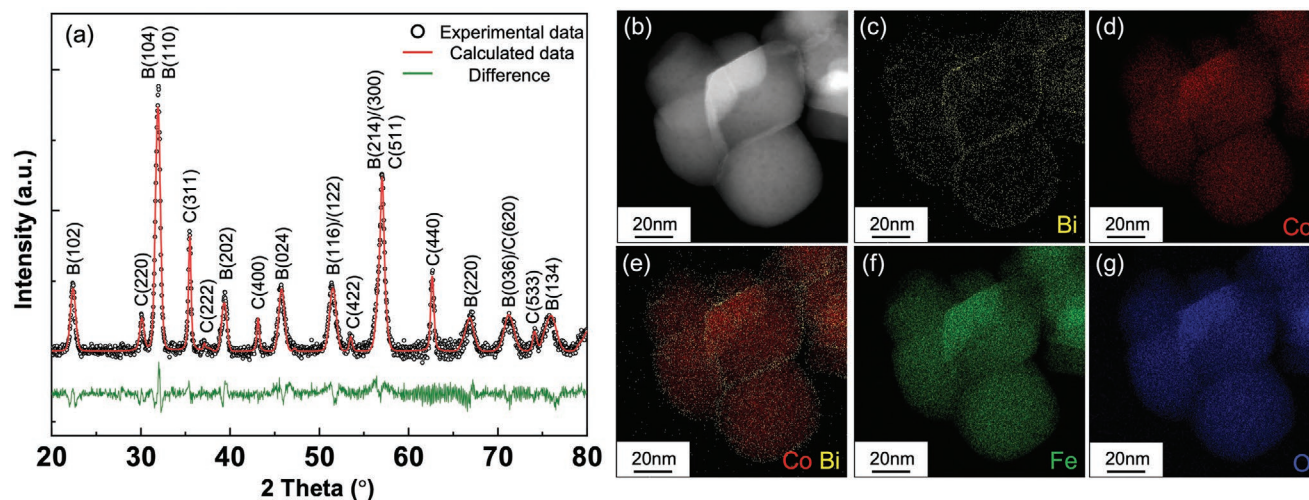


**Figure 1.** a)  $\theta$ - $2\theta$  X-ray diffraction scan and the Rietveld refinement of CFO-BFO core-shell nanoparticles. Each peak is assigned to the corresponding Bragg peaks of Fd-3m CFO and R3c BFO phases (denoted by C and B, respectively). b–g) HAADF-STEM and EDX analyses of the core-shell nanoparticles.

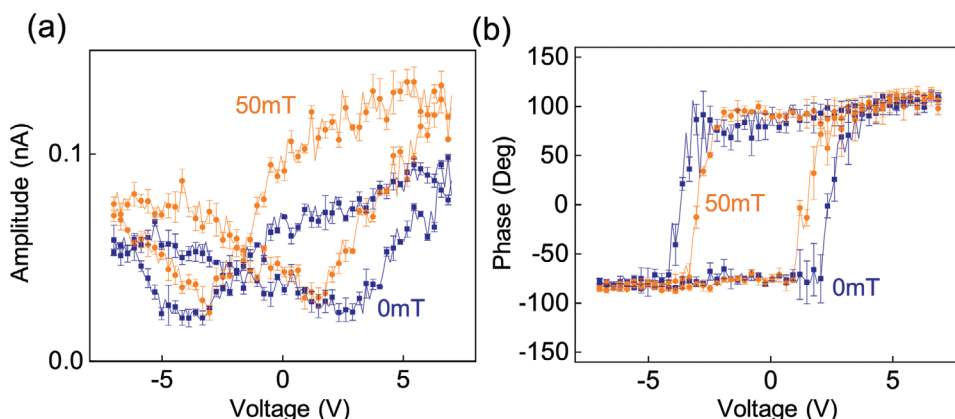


**Figure 2.** a,b) Magnetic-field-dependent local PFM hysteresis: amplitude (a) and phase (b) loops.

water/methanol, physical mixture of CFO and BFO + DI water, physical mixture of CFO and BFO + DI water/methanol) and no hydrogen evolution was observed. These results show that the hydrogen evolution is only triggered by the application of a magnetic field to the CFO–BFO core–shell nanoparticles; we therefore attribute the HER observation to the magnetoelectric effect. The magnetoelectric effect can generate charge carriers on the surface of core–shell nanoparticles, which reduce (oxidize) water molecules into hydrogen (oxygen). The low yield of the evolved hydrogen may be accounted for by rapid electron–hole recombination.<sup>[20,21]</sup> To test this possibility, we then added methanol to the DI water as methanol is known to be a reactive species scavenger to enhance the hydrogen production yield.<sup>[22,23]</sup> It has been proved by using methanol/D<sub>2</sub>O isotope water that methanol molecules do not react directly to produce hydrogen but rather consume holes generated in the catalysts.<sup>[24]</sup> As expected, with the addition of methanol (methanol:DI water = 1:9), 28.7  $\mu\text{mol g}^{-1}$  of hydrogen was produced after 6 h (Figure 3a). The effect of the magnetic field intensity and frequency on hydrogen evolution was further investigated in a methanol/DI water solution. In the given range, hydrogen evolution increased when higher intensities and frequencies were applied (Figure 3b,c), which could be attributed to the larger magnetostrictive strain transferred

to the BFO shell under higher intensities and faster kinetics under higher frequencies.

We now examine the possible mechanisms for the magneto-electrically induced HER. When a magnetic field is applied, magnetostrictive CFO responds to the magnetic field and transfers strain to the BFO shell. What remains to be clarified here is how the strain on BFO leads to changes to its electronic properties in order to promote the reaction.<sup>[25]</sup> To this aim, we performed first-principles calculations based on density functional theory (DFT). Without loss of generality, we studied a [001] oriented slab of BFO, consisting of stacks of positively charged Bi<sup>3+</sup>O<sup>2-</sup> and negatively charged Fe<sup>3+</sup>O<sup>2-</sup> layers (Figure 4a). As a result of the charged layers, BFO has unstable charged (001) surfaces<sup>[26]</sup> and the ferroelectric polarization in such a slab aligns itself so that it provides negative (positive) charges on the positive BiO (negative FeO<sub>2</sub>) surface, providing full compensation of the surface charges (Figure 4a, top).<sup>[25,27]</sup> This electrostatically stable combination of surface terminations and polarization directions results in no electric field across the slab, with the energies of the band edges independent of their layer position in the slab (see the density of states graph in Figure 4a). Slabs containing BFO (111) surfaces show the same behavior (Figure S4, Supporting Information).

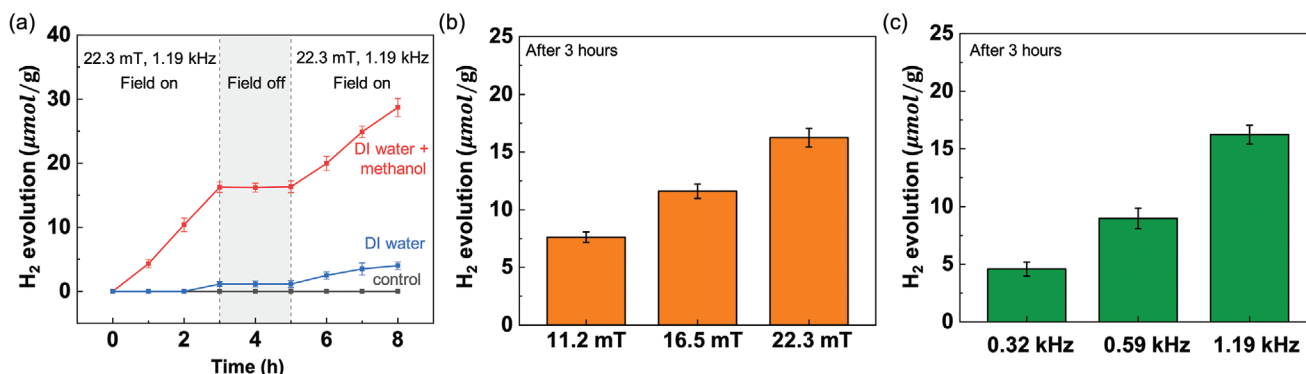


**Figure 3.** a) Hydrogen evolution measured from GC spectra under an alternating magnetic field (22 mT, 1.19 kHz) as a function of time. Control samples indicate DI water, methanol/DI water solution, CFO nanoparticles mixed with DI water, and CFO nanoparticles mixed with methanol/DI water solution. b,c) Magnetic field intensity (b) and frequency (c) dependency of hydrogen evolution (after 3 h of magnetic field application) in CFO–BFO particles mixed with methanol/DI water solution. Each data point was measured at least 3 times. The data is presented as mean value  $\pm$  the SD.

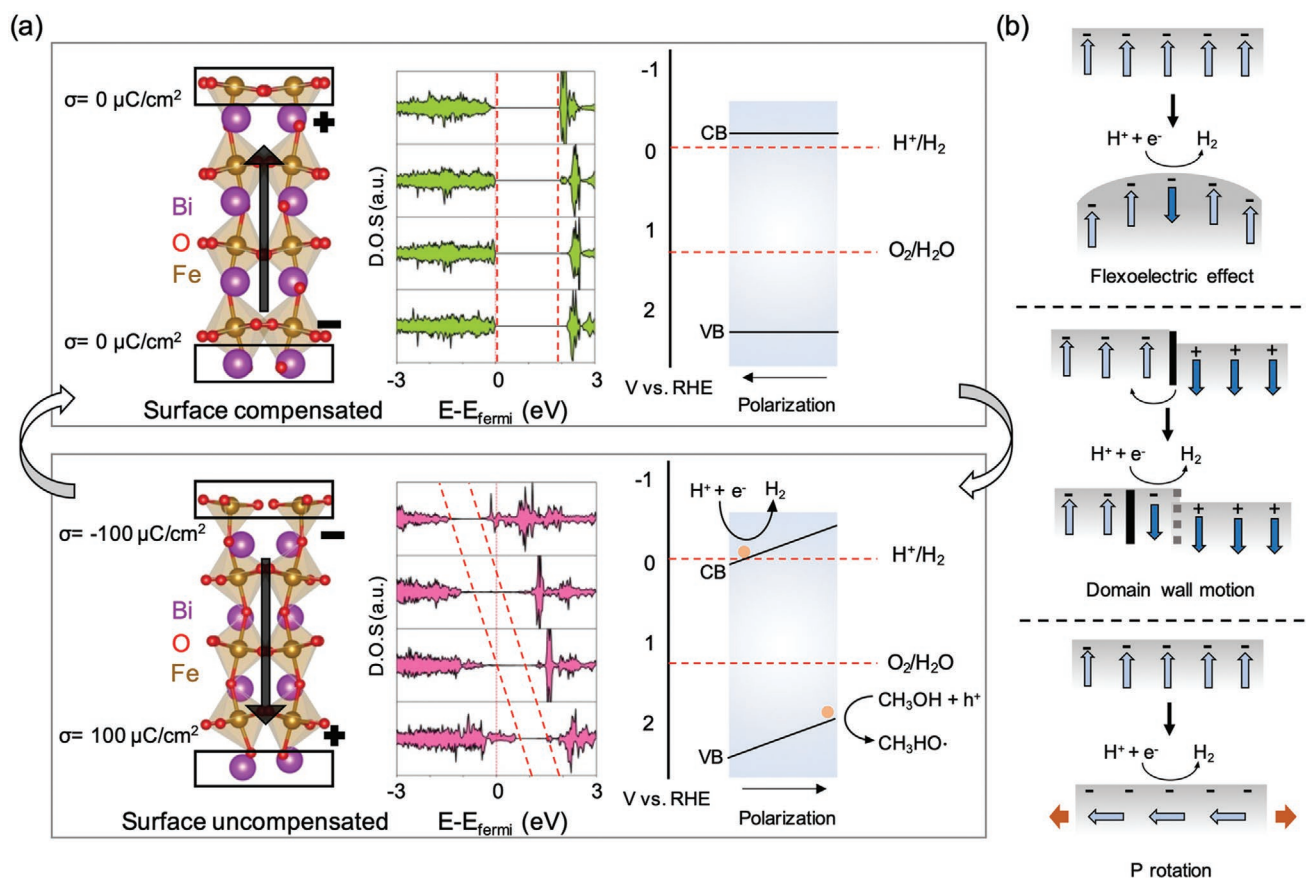


**Figure 4.** a) BFO (001) slabs used for calculation (left), the calculated layer-by-layer density of states (middle), and schematic diagrams of the band bending caused by the reversal of the polarization (right) for up-polarization (surface compensated, top) and down-polarization (surface uncompensated, bottom). b) Possible mechanisms for the polarization reversal by magnetolectric coupling in core-shell nanoparticles. (top) Generation of strain gradients leads to a flexoelectric-induced polarization reversal, (middle) strain-induced motion of domain walls, and (bottom) tensile-strain induced in-plane rotation of the polarization.

We also observed that strain does not directly change the band alignment in the slabs. Indeed, calculations (performed by varying the in-plane lattice parameters) show that the direct effect of strain on the electronic properties of BFO slabs is small as in the case of bulk BFO,<sup>[28]</sup> with negligible change to the electronic structure and band alignment (Figure S5, Supporting Information), for strains of up to  $\pm 3\%$  (The maximum strain imposed by the CFO is about 0.06%). Moreover, calculations of the adsorption and dissociation energy of water on strained BFO showed very small changes with respect to the unstrained case (Table S2, Supporting Information). Therefore, another mechanism has to be responsible for the increased catalytic activity under the magnetic field of the CFO-BFO nanoparticles. When the polarization direction of the surface compensated BFO slab is reversed, the positive (negative) end of the polarization terminates at the positive BiO (negative FeO<sub>2</sub>) surface, leading to a severe band bending (Figure 4a, bottom). As a result, the valence band maximum of the positive BiO surface shifts above the Fermi level, and the conduction band minimum of the negative FeO<sub>2</sub> surface shifts below the Fermi level, “providing” charges at both surfaces. To verify that electrons are indeed generated on the CFO-BFO

nanoparticle surfaces under magnetic field, we dispersed CFO-BFO nanoparticles in AgNO<sub>3</sub> solution and applied an AC magnetic field. After the field application, Ag nanoparticles were deposited around the CFO-BFO nanoparticles, which clearly indicate the generation of electrons at the BFO surfaces (Figure S6, Supporting Information). Based on Mott-Schottky measurement, it can be inferred that the conduction band minima of CFO-BFO nanoparticles are located slightly above the hydrogen potential (Figure S7, Supporting Information). Therefore, we can conclude that when the direction of polarization reverses and band bending occurs, the electrons generated on the surface of BFO can participate in the HER (Figure 4a).

In the literature, strain-driven polarization direction changes have been observed in ferroelectric materials via a variety of mechanisms. In Figure 4b, we show schematically three likely mechanisms, which could all occur in the CFO-BFO nanoparticles: i) If strain gradients are generated in the BFO shell by the magnetostriction of CFO, the flexoelectric effect could cause local switching of the polarization.<sup>[29,30]</sup> ii) In a polydomain BFO shell, the different orientations of the polarization domains will be next to each other. For example, as shown in the middle of

Figure 4b, neighboring patches of BFO (001) with BiO and FeO<sub>2</sub> surface termination are likely to occur. By means of strain, the domain walls separating these patches could move and create local polarization reversal.<sup>[31–33]</sup> iii) It has been shown that in-plane strain can create a preference for the ferroelectric polarization direction: perpendicular to the surface for compressive strain and parallel to the surface for tensile strain.<sup>[34]</sup> Rotation of the ferroelectric polarization to the direction parallel to the surface would lead to polar surfaces, since the charge coming from the ionic layers is left uncompensated.

### 3. Conclusions

We have demonstrated the use of magnetic fields as a trigger for renewable energy harvesting by exploiting the magneto-electric effect via CFO–BFO core–shell nanoparticles that can clearly act as HER catalyst. We propose a mechanism that when a magnetic field is applied, the magnetostrictive CFO core responds to the field and transfers the strain to the BFO shell, causing changes in the BFO ferroelectric polarization direction. The reversal of the polarization caused by the magnetoelectric coupling results in charge generation at the particle surface, which would be the driving force for the magneto-electrically induced catalytic reactions. The large penetration depth of magnetic fields allows complex catalytic architectures to be fully activated in opaque water media where light hardly reaches to initiate photocatalysis. We believe that our findings could provide cooperative pathways for maximizing hydrogen production yield by synergetic combinations of magnetic fields with other energy sources.

### 4. Experimental Section

**Nanoparticles Synthesis:** CoFe<sub>2</sub>O<sub>4</sub>–BiFeO<sub>3</sub> core–shell nanoparticles were synthesized using co-precipitation, hydrothermal, and sol–gel processes as previously reported.<sup>[13]</sup> 2 g of CTAB was dissolved in 30 mL of DI water and afterward 1 g of FeCl<sub>3</sub> 6H<sub>2</sub>O and 0.24 g CoCl<sub>2</sub> anhydrous powders were dissolved. Subsequently, 6 M NaOH solution was carefully mixed with chemical solution to precipitate CFO nanoparticles. To make CFO nanoparticles single-crystalline, chemical solution was sealed in an autoclave and treated at high temperature for a hydrothermal process. BFO shell was coated by sol–gel process. 0.243 g of Fe(NO<sub>3</sub>)<sub>3</sub> 9H<sub>2</sub>O and 0.322 g of Bi(NO<sub>3</sub>)<sub>3</sub> 5H<sub>2</sub>O were dissolved in 60 mL of ethylene glycol solution and mixed with 0.1 g of as-synthesized CFO nanoparticles. Then the mixture was heated up to 80 °C and dried overnight. Dried powder was annealed at 600 °C to crystallize the BFO shell.

**Materials Characterizations:** The crystallinity of synthesized nanoparticles was measured with an X-ray diffractometer (Bruker AXS D8 Advance), equipped with Lynxeye superspeed detector. Transmission electron microscopy (TEM), scanning transmission electron microscopy (STEM), and energy-dispersive X-ray spectroscopy (EDX) were performed with FEI Talos F200X. Piezoelectric properties and magnetoelectric coupling were measured with piezoresponse force microscopy (ND-MDT) equipped with an in-plane DC magnetic field setup. A Au-coated conductive tip was used in contact mode in order to apply an alternating voltage and induce piezoelectric oscillations. The local piezoelectric hysteresis loop was measured by applying DC voltage superimposed with small AC voltage and averaged after 5 times measurements. For electrochemical Mott–Schottky analysis, 3 mg of CFO–BFO nanoparticles were dispersed in 10 μL Nafion + 10 μL

ethanol solution and drop-cast on a conductive ITO glass (cured at 60 °C in a vacuum oven). A carbon rod and Ag/AgCl electrode were used as a counter and reference electrode, respectively, with 0.5 M Na<sub>2</sub>SO<sub>4</sub> electrolyte. For Ag nanoparticles deposition, 10 mg of CFO–BFO nanoparticles were dispersed in 10 mL of 50mM AgNO<sub>3</sub> solution and 22.3 mT, 1.19 kHz AC magnetic field was applied for 1 h. The particles were then cleaned with acetone, isopropyl alcohol (IPA), and DI water several times and collected for TEM measurements.

**Hydrogen Evolution Measurement:** 10 mg of as-synthesized CFO–BFO core–shell nanoparticles were dispersed in 10 mL of DI water and 9 mL/1 mL of DI water/methanol solution. Magneto-electrically induced HER was monitored with an online GC setup. The reaction chamber was directly connected to GC (Shimadzu GC 2014) and the pressure and the temperature of the system were carefully monitored during the reaction. High purity Ar gas was used as both carrier gas and flushing gas. Before applying magnetic fields, the whole system was flushed with Ar for 5 min to remove any other gases remaining in the system. After the reaction, a valve connecting to GC column was opened and 10 μL of gas was injected into GC and analyzed.

**DFT Calculation:** DFT calculations were performed within the periodic supercell approach using the Vienna Ab initio Simulation Package (VASP) code.<sup>[35–38]</sup> The optB86b-vdW functional,<sup>[39]</sup> a revised version of the van der Waals (vdW) density functional of Dion et al.,<sup>[40]</sup> was chosen for the calculations because it has been shown to describe molecular adsorption on transition metal oxides well.<sup>[41–43]</sup> Effective on-site interactions for the localized d-orbitals of Fe atoms were considered by adding a Hubbard *U* term in the Dudarev approach<sup>[44]</sup> with *U* – *J* = 4.0 eV. Core electrons were replaced by projector augmented wave (PAW) potentials,<sup>[45]</sup> while the valence states (5 e<sup>–</sup> for Bi, 8 e<sup>–</sup> for Fe, and 6 e<sup>–</sup> for O) were expanded in plane waves with a cut-off energy of 500 eV. The unit cell of the calculated bulk structure has a surface area of  $\sqrt{2}a \times \sqrt{2}a$  and height of *2a*, where *a* is the lattice parameter of pseudocubic unit cell. The pseudocubic lattice parameter was calculated to be *a* = 3.95 Å, with the  $\gamma$  angle in the rhombohedral structure being  $\gamma = 90.23^\circ$  by using the optB86b-VdW functional. The difference in the calculated lattice parameters with respect to the experimental structure was below 0.5%.<sup>[46]</sup> A Monkhorst–Pack k-point grid of (5×5×1) was used for all calculations. For the density of states calculations, a Monkhorst–Pack k-point grid of 7×7×1 was used. An antiferromagnetic G-type ordering was imposed, which gave a magnetic moment of 4.15 μ<sub>B</sub> per Fe ion in the bulk BFO. The BFO (001) slabs built for water adsorption had a thickness of 4 unit cells and were separated from their periodic repetitions in the direction perpendicular to the surface by ≈20 Å of vacuum. In the previous work, it was found that this thickness was sufficient to converge the adsorption energies of the water molecules.<sup>[25]</sup> A dipole correction along the direction perpendicular to the surface was applied and geometry optimizations were performed with a residual force threshold of 0.01 eV Å<sup>–1</sup>. To investigate the impact of biaxial epitaxial strain on water adsorption, the in-plane lattice parameters of BFO (001) were fixed to the corresponding lattice parameter value with the respectively applied misfit strain by the relation

$$\text{Misfit } f = \frac{a_{f,\text{strained}} - a_{f,\text{relaxed}}}{a_{f,\text{strained}}} \quad (1)$$

where *a*<sub>*f*,strained</sub> denotes the strained lattice parameter and *a*<sub>*f*,relaxed</sub> the relaxed bulk lattice parameter. Thus, the negative value of the misfit strain shows compressive strain while the positive value shows the tensile strain. For all different systems, a range of from –3% to +3% strain values were used.

Adsorption energies for the water molecules, *E*<sub>ads</sub>, were calculated as

$$E_{\text{ads}} = \frac{(E_{\text{water/BFO}} - E_{\text{BFO}} - nE_{\text{water}})}{n} \quad (2)$$

where *E*<sub>BFO</sub>, *E*<sub>water</sub>, and *E*<sub>water/BFO</sub> are the total energies of the relaxed bare slab, an isolated gas phase water molecule, and a system containing *n* water molecules adsorbed on the slab, respectively. Negative values of

the adsorption energy indicate favorable (exothermic) adsorption. Water coverages varying between  $\frac{1}{2}$  and 1 monolayer (ML)-where 1 ML is one water molecule per surface metal atom- were considered. The projected density of states for each atom was calculated in the slab and summed up the contributions for atoms in each BiFeO<sub>3</sub> bilayer. Polarization along the [001] direction was calculated by computing the displacement of each ion from the high symmetry position and multiplying it by the Born effective charges.<sup>[47]</sup>

**Statistical Analysis:** Each data point in the hydrogen evolution experiments was measured at least 3 times. The data were presented as mean  $\pm$  standard deviation (SD).

## Supporting Information

Supporting Information is available from the Wiley Online Library or from the author.

## Acknowledgements

This work has been financed by the ERC Consolidator Grant “Highly Integrated Nanoscale Robots for Targeted Delivery to the Central Nervous System” HINBOTS under the grant no. 771565 and MSCA-ITN training programme “mCBEs” under the grant no. 764977. X.C. would like to acknowledge the Swiss National Science Foundation (No. CRSK-2\_190451) for partial financial support. The gas chromatograph test station used in this work was funded by the Swiss National Science Foundation program R’Equip project no. 121306. The authors would also like to thank the Scientific Center for Optical and Electron Microscopy (ScopeM) and FIRST laboratory at ETH for their technical support. C.G. was supported by the European Union’s horizon 2020 research and innovation program under the Marie Skłodowska-Curie Grant Agreement No. 744027. N.A.S. acknowledges funding from the European Research Council (ERC) under the European Union’s Horizon 2020 research and innovation program (Grant Agreement No. 810451). Calculations were performed on the Euler cluster managed by the HPC team at ETH Zurich and the Swiss National Supercomputing Center (CSCS) under Project No. s889. J.P-L also acknowledges support from European Research Council Starting Grant microCrysFact (ERC-2015-STG No. 677020), the Horizon 2020 FETOPEN project SPRINT (No.801464), the Swiss National Science Foundation (project no. 200021\_181988), and grant PID2020-116612RB-C33 funded by MCIN/AEI /10.13039/501100011033.

Open access funding provided by Eidgenössische Technische Hochschule Zurich.

## Conflict of Interest

The authors declare no conflict of interest.

## Data Availability Statement

The data that support the findings of this study are available from the corresponding author upon reasonable request.

## Keywords

energy harvesting, hydrogen evolution, magnetoelectric coupling, multiferroics

Received: December 28, 2021

Revised: February 12, 2022

Published online: March 28, 2022

- [1] Y. Zhang, C. Liang, J. Wu, H. Liu, B. Zhang, Z. Jiang, S. Li, P. Xu, *ACS Appl. Energy Mater.* **2020**, *3*, 10303.
- [2] M. J. Jacinto, L. F. Ferreira, V. C. Silva, J. Sol-Gel Sci. Technol. **2020**, *96*, <https://doi.org/10.1007/s10971-020-05333-9>.
- [3] Q. Yang, J. Du, X. Nie, D. Yang, L. Bian, L. Yang, F. Dong, H. He, Y. Zhou, H. Yang, *ACS Catal.* **2021**, *11*, 1242.
- [4] K. Akbar, S. Hussain, L. Truong, S. B. Roy, J. H. Jeon, S.-K. Jerng, M. Kim, Y. Yi, J. Jung, S.-H. Chun, *ACS Appl. Mater. Interfaces* **2017**, *9*, 43674.
- [5] C. Niether, S. Faure, A. Bordet, J. Deseure, M. Chatenet, J. Carrey, B. Chaudret, A. Rouet, *Nat. Energy* **2018**, *3*, 476.
- [6] U. Gupta, C. R. Rajamathi, N. Kumar, G. Li, Y. Sun, C. Shekhar, C. Felser, C. N. R. Rao, *Dalton Trans.* **2020**, *49*, 3398.
- [7] O. Sambalova, E. Billeter, O. Yildirim, A. Sterzi, D. Bleiner, A. Borgschulte, *Int. J. Hydrogen Energy* **2021**, *46*, 3346.
- [8] W. Zhou, M. Chen, M. Guo, A. Hong, T. Yu, X. Luo, C. Yuan, W. Lei, S. Wang, *Nano Lett.* **2020**, *20*, 2923.
- [9] F. A. Garcés-Pineda, M. Blasco-Ahicart, D. Nieto-Castro, N. López, J. R. Galán-Mascarós, *Nat. Energy* **2019**, *4*, 519.
- [10] X. Ren, T. Wu, Y. Sun, Y. Li, G. Xian, X. Liu, C. Shen, J. Gracia, H.-J. Gao, H. Yang, Z. J. Xu, *Nat. Commun.* **2021**, *12*, 2608.
- [11] N. A. Spaldin, *Proc. R. Soc. A* **2020**, *476*, 20190542.
- [12] D. K. Pradhan, S. Kumari, P. D. Rack, *Nanomaterials* **2020**, *10*, 2072.
- [13] F. Mushtaq, X. Chen, H. Torlakcik, C. Steuer, M. Hoop, E. C. Siringil, X. Marti, G. Limburg, P. Stipp, B. J. Nelson, S. Pané, *Adv. Mater.* **2019**, *31*, 1901378.
- [14] X.-Z. Chen, N. Shamsudhin, M. Hoop, R. Pieters, E. Siringil, M. S. Sakar, B. J. Nelson, S. Pané, *Mater. Horiz.* **2016**, *3*, 113.
- [15] G. Srinivasan, *Annu. Rev. Mater. Res.* **2010**, *40*, 153.
- [16] C. M. Leung, J. Li, D. Viehland, X. Zhuang, *J. Phys. D: Appl. Phys.* **2018**, *51*, 263002.
- [17] R. M. Bozorth, E. F. Tilden, A. J. Williams, *Phys. Rev.* **1955**, *99*, 1788.
- [18] K. Venkata Siva, S. Sudersan, A. Arockiarajan, *J. Appl. Phys.* **2020**, *128*, 103904.
- [19] H. Miao, X. Zhou, S. Dong, H. Luo, F. Li, *Nanoscale* **2014**, *6*, 8515.
- [20] Y. M. Sheu, S. A. Trugman, Y. S. Park, S. Lee, H. T. Yi, S. W. Cheong, Q. X. Jia, A. J. Taylor, R. P. Prasankumar, *Appl. Phys. Lett.* **2012**, *100*, 242904.
- [21] D. Kim, H. Han, J. H. Lee, J. W. Choi, J. C. Grossman, H. M. Jang, D. Kim, *Proc. Natl. Acad. Sci. USA* **2018**, *115*, 6566.
- [22] J. T. Schneider, D. S. Firak, R. R. Ribeiro, P. Peralta-Zamora, *Phys. Chem. Chem. Phys.* **2020**, *22*, 15723.
- [23] X. Xu, L. Xiao, Y. Jia, Z. Wu, F. Wang, Y. Wang, N. O. Haugen, H. Huang, *Energy Environ. Sci.* **2018**, *11*, 2198.
- [24] F. Guzman, S. S. C. Chuang, C. Yang, *Ind. Eng. Chem. Res.* **2013**, *52*, 61.
- [25] I. Efe, N. A. Spaldin, C. Gattinoni, *J. Chem. Phys.* **2021**, *154*, 024702.
- [26] M. Stengel, *Phys. Rev. B* **2011**, *84*, 205432.
- [27] N. A. Spaldin, I. Efe, M. D. Rossell, C. Gattinoni, *J. Chem. Phys.* **2021**, *154*, 154702.
- [28] C. Ederer, N. A. Spaldin, *Phys. Rev. Lett.* **2005**, *95*, 257601.
- [29] H. Lu, C. W. Bark, D. Esque de los Ojos, J. Alcalá, C. B. Eom, G. Catalan, A. Gruverman, *Science* **2012**, *336*, 59.
- [30] L. Chen, Z. Cheng, W. Xu, X. Meng, G. Yuan, J. Liu, Z. Liu, *Sci. Rep.* **2016**, *6*, 19092.
- [31] E.-J. Guo, R. Roth, A. Herklotz, D. Hesse, K. Dörr, *Adv. Mater.* **2015**, *27*, 1615.
- [32] M. D. Biegalski, D. H. Kim, S. Choudhury, L. Q. Chen, H. M. Christen, K. Dörr, *Appl. Phys. Lett.* **2011**, *98*, 142902.
- [33] M. Slabki, L. Kodumudi Venkataraman, S. Checchia, L. Fulanović, J. Daniels, J. Koruza, *Phys. Rev. B* **2021**, *103*, 174113.
- [34] M. F. Sarott, M. Fiebig, M. Trassin, *Appl. Phys. Lett.* **2020**, *117*, 132901.
- [35] G. Kresse, J. Hafner, *Phys. Rev. B* **1993**, *47*, 558.
- [36] G. Kresse, J. Hafner, *Phys. Rev. B* **1994**, *49*, 14251.

- [37] G. Kresse, J. Furthmüller, *Comput. Mater. Sci.* **1996**, *6*, 15.
- [38] G. Kresse, J. Furthmüller, *Phys. Rev. B* **1996**, *54*, 11169.
- [39] J. Klimeš, D. R. Bowler, A. Michaelides, *Phys. Rev. B* **2011**, *83*, 195131.
- [40] M. Dion, H. Rydberg, E. Schröder, D. C. Langreth, B. I. Lundqvist, *Phys. Rev. Lett.* **2004**, *92*, 246401.
- [41] S. Dabaghmanesh, E. C. Neyts, B. Partoens, *Phys. Chem. Chem. Phys.* **2016**, *18*, 23139.
- [42] J. K. Roy, S. Kar, J. Leszczynski, *Sci. Rep.* **2018**, *8*, 10997.
- [43] A. Lozano, B. Escibano, E. Akhmatkaya, J. Carrasco, *Phys. Chem. Chem. Phys.* **2017**, *19*, 10133.
- [44] S. L. Dudarev, G. A. Botton, S. Y. Savrasov, C. J. Humphreys, A. P. Sutton, *Phys. Rev. B* **1998**, *57*, 1505.
- [45] G. Kresse, D. Joubert, *Phys. Rev. B* **1999**, *59*, 1758.
- [46] F. Kubel, H. Schmid, *Acta Crystallogr. B* **1990**, *46*, 698.
- [47] J. B. Neaton, C. Ederer, U. V. Waghmare, N. A. Spaldin, K. M. Rabe, *Phys. Rev. B* **2005**, *71*, 014113.